The following document is pending Distribution A approval. The document shall not be distributed unless it has been stamped as Cleared for Open Publication by the Office of Prepublication and Security Review.

Scaling Sensitivity of Focused Laser Differential Interferometry Across Facilities

Paul Medina

A thesis
submitted in partial fulfillment of the
requirements for the degree of

Master of Science in
Aeronautics and Astronautics

University of Washington

2025

Committee:

Owen J. H. Williams

Pino M. Martin

Program Authorized to Offer Degree:
Aeronautics and Astronautics

University of Washington

Abstract

Scaling Sensitivity of Focused Laser Differential Interferometry Across Facilities

Paul Medina

Chair of the Supervisory Committee:
Owen J. H. Williams
Aeronautics & Astronautics

Focused Laser Differential Interferometry (FLDI) is a novel technique that leverages optical interference to measure index of refraction and hence density gradients within high-speed fluids. This technique provides excellent spatial and temporal resolution compared to traditional measurement techniques by offering a non-intrusive diagnostic with fast sample rates (> 1 MHz). Its sensitivity; however, is limited to a narrow range of frequencies and length scales, which depend on the optical elements used and their relative distances. This thesis investigates how the signal response of FLDI changes with the size of a wind tunnel facility. The goal is to alter the optical elements to achieve the same sensitivity across facilities so that data can be directly compared and the underlying physics evaluated. Analytical FLDI transfer functions are adapted from literature to model the theoretical signal response of FLDI. This modeling provides insight into how component variations affect scaling for wind tunnels of three sizes, representative of small labs to national facilities. In this study, optical components are selected after optimization with the

theoretical FLDI transfer functions for the three facility scales, ranging from test section diameters of 1 ft to 4 ft. Theoretical optimization shows that scaling optical components can match the FLDI signal response between facilities. However, larger facilities necessitate greater splitting angles between the orthogonal beams, which decreases the instrument's spatial resolution. Further, this thesis examines FLDI sensitivity relative to dominant flow features present from high-speed jet-interactions; with the goal of analyzing FLDI's response compared to its analytical sensitivity. This work highlights the challenge of comparing FLDI data between different wind tunnel facilities, while also particularly emphasizing the importance of considering the transfer functions and sensitivities of the setup of FLDI used in experiments.

TABLE OF CONTENTS

LIST OF FIGURES

LIST OF TABLES

NOMENCLATURE

St: Strouhal number
f: Frequency
k: Wavenumber
d: Diameter
U: Velocity
M: Mach number
P: Pressure of fluid
T: Temperature of fluid
I: Jet momentum ratio
ρ: Density of fluid
Δx: Beam separation distance of FLDI
F: Field lens
ϵ: Wollaston prism splitting angle
$\omega(z)$: Beam radius along beam path
ω_0: Beam radius at focus
λ_0: Laser beam wavelength
z: Beam path
S: Distance between lenses
f: Focal length
E: Laser beam intensity
E_{PD}: Intensity incident on photodetector
$\Delta\phi$: Phase difference between FLDI beams
$\Delta\phi_0$: Phase difference offset
V: Voltage
H: FLDI transfer functions
H_{PD}: Photodetector transfer function
n: Index of refraction
K: Gladstone-Dale constant
X_{SR}: x-direction spatial resolution
Y_{SR}: y-direction spatial resolution
Z_{SR}: z-direction spatial resolution
α: Convective flow angle in xy-plane

ACKNOWLEDGMENTS

I would like express my extreme gratitude to my advisor, Dr. Owen Williams and reader, Dr. Pino Martin for providing much need guidance and support as well for accommodating my condensed timeline. I would further like to extend my thanks to the whole UCAH team, especially: Dr. Richard Miles, Lake Larson, Brady Black, Jack Ninos, and Haris Mahmood for aiding throughout every step of implementing FLDI at Texas A&M. Lastly, I would like to thank Mathew Rheney and Jacob Vaughn for the many hours running the wind tunnel, and John Kochan and Nathan Jergens for setting us up in the National Aerothermochemistry Laboratory.

DEDICATION

This thesis is dedicated to my parents, Elisa and Douglas Medina.

Chapter 1
INTRODUCTION

Improving control of high-speed vehicles stands among today's most formidable engineering challenges. At high Mach number, vehicles are notoriously difficult to control with conventional flight control surfaces. To provide control, reacting jets are an innovative method, providing rapid and large control forces. Even so, reacting jets themselves are problematic, since they change the pressure distribution, side force, and heat transfer around the vehicle due to the complex interactions with the incoming flow and boundary layer. As a result, the forces expected due to the thrust of the jet can be vastly different in flight. These instabilities in the flowfield occur at a wide range of frequencies due to their presence near shocks and jet-interaction vortices. To gain a better understanding of these instabilities, uncovering the frequencies off-body of reacting jets at various Mach numbers is imperative. One measurement technique that can non-intrusively measure point-like index of refraction and hence density fluctuations at high rate is Focused Laser Differential Interferometry (FLDI). This technique interferes two focused beams which are spatially separated by a small distance, Δx, in the center of the test section. The spatially separated and focused beams attenuate high wavenumbers faster than low wavenumbers and create a band-pass filtering effect centered at high wavenumbers. Although FLDI is widely used in high-speed wind tunnels, little research has attempted to match wavenumber response across a range of flow and facility size. This thesis intends to illuminate the challenges with matching spatial and wavenumber resolution of FLDI across scales of facilities; while also implementing FLDI into a wind tunnel to probe high-speed jets in cross-flow to examine the issues when FLDI is overly sensitive to wavenumbers not present in the flow phenomena.

Jets in cross-flow have been the subject of study for decades. Early experiments have successfully documented the time-averaged velocity fields of supersonic jets in cross-flow as detailed in Mahesh's Annual Reviews article [3]. Studies, such as from Viti *et al* [4], have shown that the flow field is dominated by streamwise counter-rotating and horseshoe vortices. Both are annotated by bullets 11 & 12 in Figure 1.1. Besides vortex formation in the jet-interaction, sharp discontinuities from the various shocks significantly affect the pressure gradients on and around the jet - all of which make this problem challenging when attempting to assess its unsteady behavior. As pointed out by Miller *et al* [1], the unsteady behavior of jets in supersonic cross-flow, not shown by time-averaged results, can significantly perturb the reacting force of a jet. Specifically, Miller *et al* proposed that unsteady shedding of shear-layer vortices that exist in the region between the barrel shock (bullet 3) and bow shock (bullet 4) as shown in Figure 1.1 and Figure 1.2, induce high pressure regions on the surface which contribute significantly to the control force of the jet [1]. Shear-layer vortex shedding is a an important element of jet-interaction due to its high frequency and instability as pointed out by Mahesh [3] - understanding the mechanisms of this unsteady behavior is critical to the design of aerospace vehicles. Other features of jet-interaction such as counter-rotating vortex pairs and horseshoe vortices play a similarly significant role inducing pressure distributions on the surface and augmenting the control force of the jet. However, shear-layer vortex shedding is interesting to study instead since wind tunnel experiments have been largely unable to provide time-resolved data of this behavior due to its unsteadiness and high frequency.

One of the most critical parameters to quantifying the unsteady behavior of shear-layer vortex shedding is the jet Strouhal number, here defined as $St_j = \frac{f\,d_j}{U_j}$ where d_j is the jet diameter and U_j is the jet velocity. Other methods for defining Strouhal number utilize the freestream velocity, but for comparison between literature, the jet velocity will be used here. The Strouhal number is a dimensionless value that quantifies the unsteady frequencies of the flow with respect to the inertial forces and physical size of the jet. With matched freestream conditions and momentum ratios, the comparison of Strouhal numbers between jet configurations allows the direct comparison of shear-layer vortex shedding behavior due to jet diameter and velocity. Current research from Miller *et al* [1] has shown that the Strouhal number of shear-layer vortex shedding scales with Mach number and jet momentum ratio, here defined as $I = \frac{\rho_j U_j^2}{\rho_\infty U_\infty^2}$. Strouhal number has also been shown to change between laminar and turbulent boundary layers. As a gauge, Ben-Yakar *et al* [5] reported jet-interaction Strouhal numbers of $St_j \approx 1$ for a turbulent boundary layer flat plate with $M_\infty = 3.4$ and $I = 4.1$. In this case, simulations resolved the shear-layer vortices one jet diameter above the jet outlet. Conversely, Miller *et al* [1] found jet-interaction Strouhal numbers of $St_j \approx 0.4$ for a laminar boundary flat plate with $M_\infty = 5$ and $I = 5.3$. Here, simulations resolved the the shear-layer vortices three jet diameters above the jet outlet.

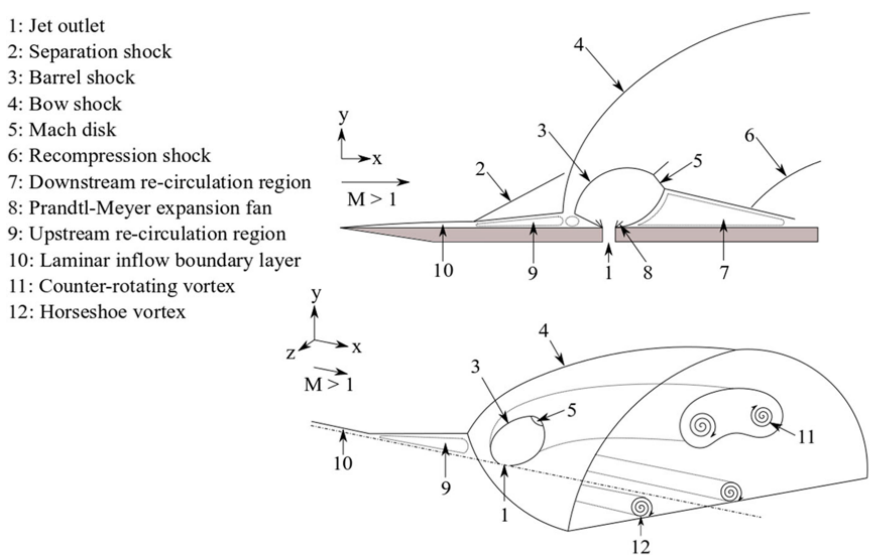

Figure 1.1: Schematic of time-averaged jet in supersonic cross-flow. The location of the shear-layer is in-between the Bow Shock (3) and the Barrel shock (4). Adapted from Miller [1]. Reprinted with Permission from AIP Publishing.

The parameter space for jet-interaction is extremely expansive as mentioned by Mahesh [3]. At high Mach number, the jet-interaction depends on momentum ratio, Mach number, and pressure, density, and temperature ratios. Specifically, the jet momentum and pressure ratio have a profound effect on jet penetration and trajectory and hence the location and frequencies present in the shear-layer. While some literature has examined various gases [6], the parameter space needs to be explored more with varying Mach numbers, gasses, and momentum ratios. Exploring this parameter space using FLDI is a significant contribution by providing time-resolved data of shear-layer vortex shedding that would otherwise be troublesome to acquire experimentally.

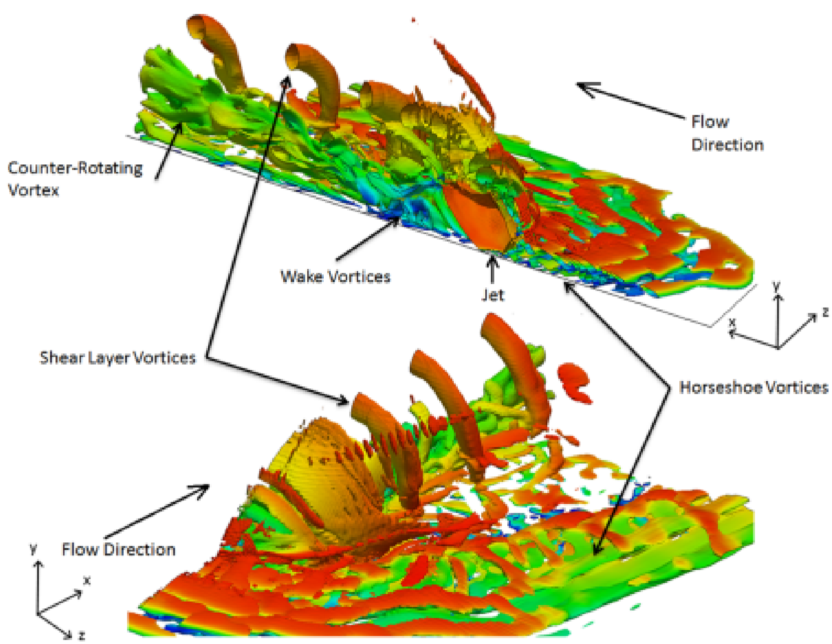

Figure 1.2: Computational rendering of jet in cross-flow at $M_\infty = 5$ and $I = 5.3$. Isometric contours of the Q-criterion plotted with distinct shear-layer, counter-rotating, and horseshoe vortices downstream of the jet. Adapted from Miller [1]. Reprinted with permission from AIP Publishing.

Measuring statistics in high-speed flows is incredibly difficult due to unsteady dynamics, high temperatures, and compressibility effects. Typically, aerodynamicist's have relied on computation fluid dynamics (CFD) to determine turbulent statistics of flow phenomena away from the surface or have utilized intrusive experimental measurement techniques such as hot-wire anemometry. In high-speed wind tunnel experiments, impingement on the flow from invasive techniques is undesirable due to the formation of bow shocks off the face of the probes which can impede true flow phenomena around the body of interest. In these regimes, both a high degree of temporal and spatial resolution is required for the measurement of turbulence statistics due to small diameter tunnels and short duration test times. With this in mind, Focused Laser Differential Interferometry, or FLDI, provides an alternative, non-intrusive diagnostic technique that allows the probing of index of refraction fluctuations off-body without disturbing the flow phenomena. FLDI was preceded by Laser Differential Interferometry (LDI) which was developed by Smeets and George [7]. The LDI system works as a shearing interferometer that uses Wollaston prisms to split a continuous-wavelength (CW) laser by a small angle into two mutually orthogonal polarizations. The mutually orthogonal polarized beams are conditioned by a field lens that ensures they travel parallel through a test section and then recombine at an identical Wollaston prism. The two beams are separated by a small distance, Δx which is set by the focal length of the field lens and Wollaston prism splitting angle. This small distance effectively allows the interferometer to measure spatially averaged index of refraction gradients at a point.

Although LDI is useful for measuring spatially averaged index of refraction gradients, Smeets and George adapted LDI by using a combination of diverging and converging optics to focus the two parallel beams to a point in the test section [8]. The resulting instrument was subsequently named Focused Laser Differential Interferometry. The additional optics improves the spatial resolution of the instrument by attenuating disturbance wavelengths smaller (high wavenumbers) than the local beam diameter as the beam travels towards its focal point. As mentioned by Schmidt and Shepherd [9], large disturbances (small wavenumbers) greater than the local beam diameter will not be attenuated away from the focus. Compared to alternative measurement techniques, FLDI provides a high degree of spatial resolution by giving a point-like measurement while also giving significant temporal resolution due to the high bandwidth of modern photodetectors which can sample at rates in the tens of MHz.

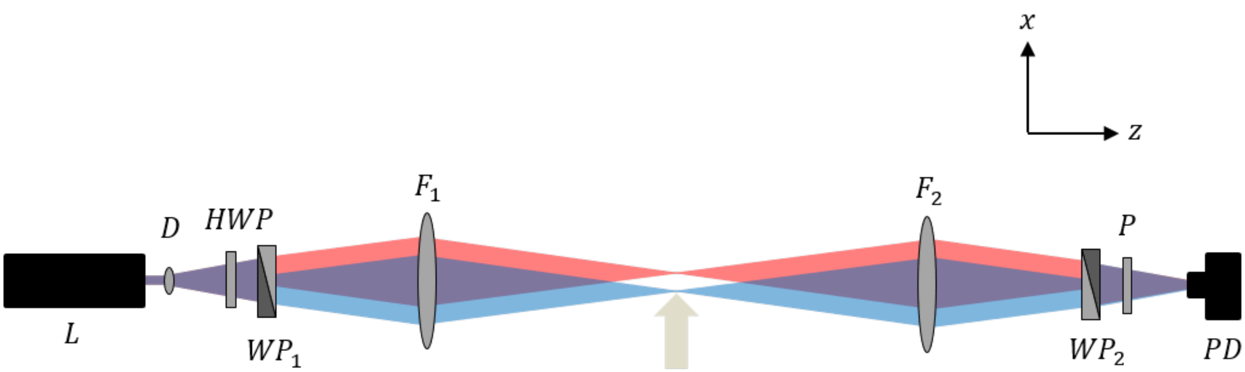

Figure 1.3: Traditional FLDI schematic showing the optics and positions of lenses. From left to right, FLDI consists of a CW laser, L, plano-concave diverging lens, D, half-wave plate, HWP, pitch side Wollaston prism, WP_1, plano-convex field lenses, F_1 and F_2, catch side Wollaston prism, WP_2, film polarizer, P_1, and photodetector, PD.

Figure 1.3 shows a typical schematic of the FLDI system. The FLDI apparatus is split into two identical sections about the focal point of the system, coined the pitch and catch side respectively. On the pitch side, the system starts with CW laser beam of low power that is first expanded by a diverging lens and polarized by a film polarizer before it is incident at 45° to the splitting axis of a Wollaston prism. The Wollaston prism splits the beam by a small angle into two mutually orthogonal polarizations states separated by a small distance or Δx. The beams are then focused by a field lens placed one focal length up-beam of the

Wollaston prism which ensures that the beams travel parallel to one another and are focused to the center of the test section. On the catch side of the system, the FLDI beams expand after reaching the focal point until an identical field lens focuses the beams back onto a catch side Wollaston prism with the same splitting angle as the first prism. A film polarizer is then placed after the catch side Wollaston prism to ensure the beams interfere. The beams are then incident on a photodetector that outputs voltage proportional to the fluctuating intensity of the interfering beams. If H_{PD} is defined as a transfer function relating the intensity of a single laser beam, E_b, to voltage - then Equation 1.1 can be used to relate phase difference to voltage where $E_b = V_b H_{PD}$ is the voltage response from a single beam. The sensitivity of an FLDI configuration is set by the beam spacing, Δx, and the focusing nature of the beams: both of which can be tuned to probe specific ranges of wavenumbers. In general, small values for Δx and sharply focused beams allow the instrument to resolve high wavenumbers only at a sensitive region around the focus; while low wavenumbers are resolved away from the focus if they have enough magnitude to evade filtering from the small beam pair spacings, Δx.

$$V = 2H_{PD}V_b[1 + \cos(\Delta\phi)] \tag{1.1}$$

In the recent literature for FLDI, a model was introduced by Parziale [10] and then subsequently expanded to transfer functions converting phase difference to index of refraction as shown by Fulghum [11] and Schmidt and Shepherd [9]. These transfer functions detail the spatial and temporal sensitivity of FLDI assuming index of refraction and hence density disturbances (via Gladstone-Dale relation) have the structure of a sinusoidal plane wave. In more recent works, Ceruzzi [12] developed a general sensitivity function that incorporates velocity variation along the beam path and convective velocity into the transfer functions. Similarly, Lawson [13] innovated the sinusoidal plane wave model to account for disturbances in three dimensions instead of solely along the x-axis.

Using the most basic form of transfer functions which assume that sinusoidal plane wave disturbances are oriented in the x-direction and that velocity does not vary along the beam path, then Equation 1.2 can be generated which quantifies FLDI sensitivity to wavenumber, k_x, and position along the beam path, z. If integrated along z, this equation can then be used as a true transfer function to relate phase difference to index of refraction, n, by Equation 1.3. Dividing by Δx then gives an approximation for the index of refraction gradient via Equation 1.4.

$$H(k_x, z) = |H_{\Delta x} H_\omega| = \sin\left(\frac{k_x \Delta x}{2}\right) \exp\left(-\frac{k_x^2 \omega_0^2}{8} - \frac{k_x^2 \lambda_0^2 z^2}{8\pi^2 \omega_0^2}\right) \tag{1.2}$$

$$\Delta\phi = n * H(k_x) \tag{1.3}$$

$$\frac{\Delta\phi}{\Delta x} \propto \frac{\partial n}{\partial x} \tag{1.4}$$

In Equation 1.2, the transfer function is split into two components: $H_{\Delta x}$ which represents the response due to the beam spacing between the two beams, and H_ω which represents the response due to the focusing of the beams. This equation shows that FLDI sensitivity is a function of laser wavelength, λ_0, beam radius at the focus, ω_0, and beam separation distance perpendicular to the optical axis, Δx. Taking a look at this equation applied in literature, Gillespie *et al* [2] applied a dual-point FLDI configuration in the University of Maryland's HyperTERP shock tunnel. The sensitivity of their instrument is given by Equation 1.2 and plotted in Figure 1.4a. The power spectrum of the phase difference from the instrument probing the nozzle shear-layer for a freestream Reynold's number of $Re_\infty = 14.4 \times 10^6\ m^{-1}$

is given in Figure 1.4b. Figure 1.4a shows that FLDI is sensitive to a narrow band of wavenumbers centered around $k_x = \pi/\Delta x$. At higher wavenumbers, the signal is attenuated by multiples of $2\pi/\Delta x$ and at lower wavenumbers, the signal is represented but uniformly filtered by producing weaker gradients along the x-direction. In their configuration, they have a sensitive wavenumber of $k_{x,sensitive} = 6756\,m^{-1}$ or a sensitive frequency of $f_{sensitive} = 945\,kHz$ when using a convective velocity of $879\,m/s$. What this shows is that for a typical FLDI configuration, as used here, the instrument is incredibly sensitive to a narrow band of high frequencies. This makes FLDI very suitable for examining jet-interaction shear-layers which are very unsteady and high frequency.

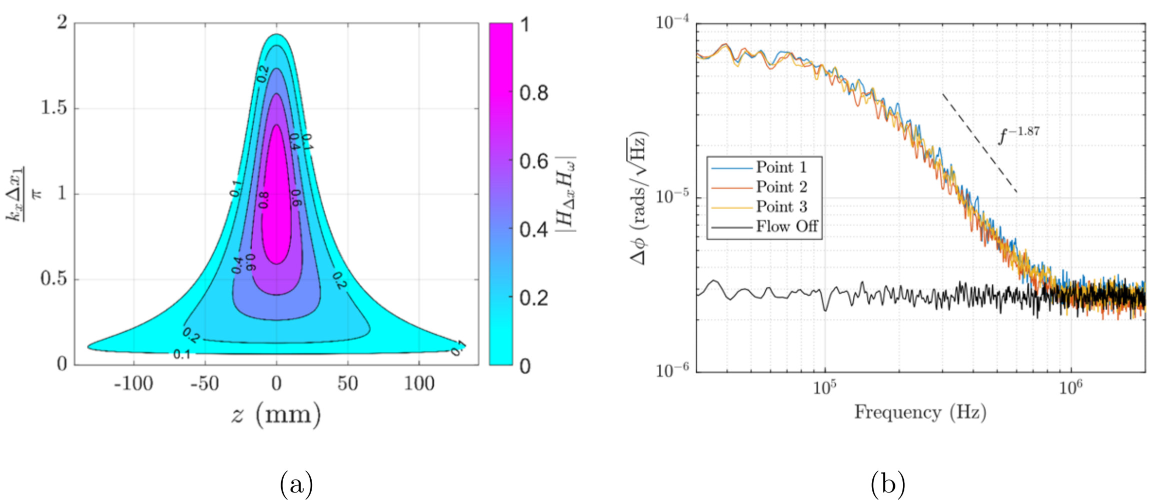

Figure 1.4: Results from Gillespie *et al* [2] showing the plotted analytical transfer function for an optical configuration with $\lambda_0 = 532\,nm$, $\omega_0 = 8.0\,\mu m$, and $\Delta x = 465\,\mu m$ and the power spectra of phase difference. This configuration utilized Dual-Point FLDI which gives a convective velocity of $879\,m/s$ and a sensitive frequency of $f_{sensitive} = 945\,kHz$. Reprinted with permission from Springer Nature.

One of the issues with FLDI, highlighted primarily by Schmidt and Shepherd [9], is that low wavenumbers are not attenuated away from the focus if their magnitudes are high. While

FLDI is very sensitive to high wavenumbers around its focus, low wavenumbers are resolved across the entire beam path. This is evident in Figure 1.4b which shows significant signal to noise at low frequencies compared to its sensitive frequency of $f_{sensitive} = 945\,kHz$. The low frequencies here are representative of the flow phenomena, but since they are not high frequencies, then they cannot be attributed with certainty to be within the region of focus - instead they are spatially averaged. This highlights the primary issue of FLDI, where the instrument is tuned for high frequencies at a sensitive region about the focus point where high frequencies do not likely exist.

Beyond developing the analytic theory of FLDI, many authors have innovated FLDI by using additional optical elements to increase the measurement bandwidth of the system. Ceruzzi [12] and Lawson [14] both pioneered Dual-Point FLDI by adding an additional Wollaston prism within the pitch side optics. This innovation is incredibly useful since it provides the ability to determine velocities through cross-correlations of each time signal; however, problems arise since the velocities are dependent on the scale of the disturbance. In other works, Davenport and Gragston [15] developed the Linear-Array technique that uses a diffractive optical element in addition to a 2nd Wollaston prism to create an $m \times n$ array of beam pairs. Further advancements have seen the use of coupled lasers of different wavelengths to probe two points along the beam axis, coined Chromatic FLDI by Webber *et al*; and cylindrical lenses used by Houpt and Leonov [16] were implemented to avoid beam clipping due to the spherically focused beams of traditional FLDI. Although impressive, the primary concern with FLDI resolving wavenumbers away from its focus is characteristic in each of these configurations; therefore, the remainder of this work will simply utilize a single-point instrument to reduce optical complexities - with the intent of examining the most sensitive region of the instrument.

The preceding discussion has shown that spatial resolution of FLDI is significant due to the focusing nature of the instrument and that its temporal resolution is on the order of 10's of MHz. However, questions remain on the wavenumber response of the instrument, and whether the transfer functions do a good job predicting the wavenumbers of greatest sensitivity. Because of this, the first objective of this thesis will be to collect experimental results for a turbulent boundary layer flat plate with a jet in high-speed cross-flow. With this experiment, the sensitivity of FLDI relative to the position of the beam pair in the shear-layer can be examined to determine if Strouhal numbers observed are spatially averaged beyond the most sensitive region about the focus or detected within it. This can be used to address FLDI's shortcomings when the Strouhal numbers of interest lie outside of the instrument's most sensitive region. Furthermore, a second FLDI configuration will be used with a repeat test case to attempt to show the variation in the instruments spatial and temporal response when optics are adjusted. The second objective of this thesis will be to theoretically apply the FLDI transfer functions to three different optical arrangements to match scaled FLDI sensitivity between typical high-speed facilities with wind tunnel diameters ranging from 1 ft to 4 ft. The conclusions of both will be useful to answer the question about what wavenumbers the instrument is measuring and with what sensitivity; and how the theoretical transfer functions can be applied to design configurations to match sensitivity between various scales of facilities.

Chapter 2

FOCUSED LASER DIFFERENTIAL INTERFEROMETRY THEORY

2.1 Basic Design & Function

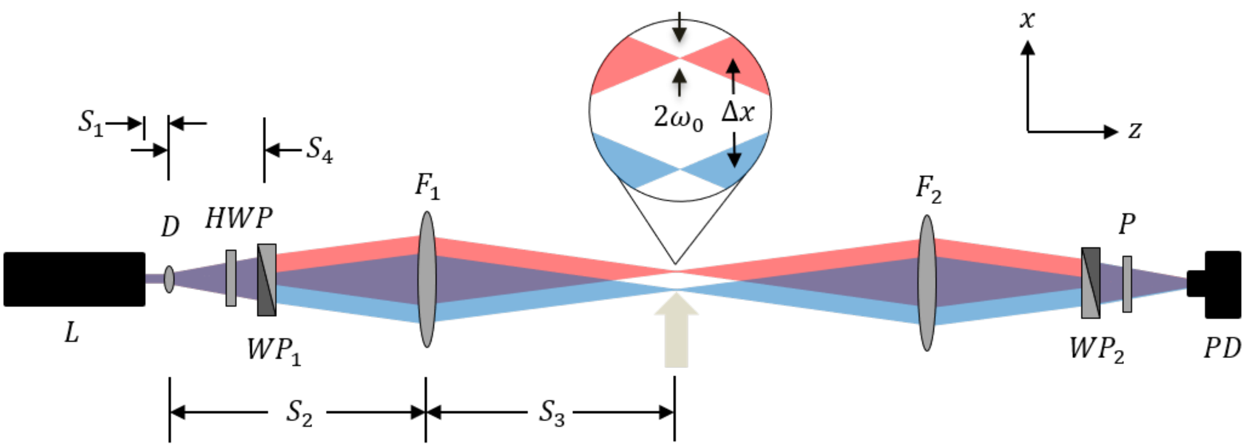

Figure 2.1: Traditional FLDI schematic showing the optics and positions of lenses. FLDI consists of a CW laser, L, a distance S_1 from the plano-concave diverging lens, D, followed by a half-wave plate, HWP. The plano-convex field lenses, F_1, is placed a distance, S_2, from the diverging lens. The Wollaston prism, WP_1, is placed a distance f_{F_1} up-beam of the field lens. The catch side field lens, F_2, and Wollaston prism, WP_2, are placed identically on the catch side of the system. The film polarizer, P_1, and photodetector, PD, are placed an arbitrary distance from the catch side Wollaston prism dependent on beam diameters.

Starting with a more comprehensive description of the optical setup of the instrument, FLDI begins with a CW laser beam of low power of around 8 - 200 mW. Low power Helium-Neon (HeNe) beams have typically been used due to their high degree of pointing stability and coherence. Higher power laser beams up to around 200 mW have been used in the literature by Lawson [14] to achieve a high signal-to-noise (SNR) ratio and in multi-point techniques to provide sufficient incident power on multiple photodetectors [17]. On the pitch side, the laser beam is first expanded by a diverging lens, D, with a short focal length, f_D, and is placed at an arbitrary distance, S_1, away from the laser. This distance is typically unimportant due to the small divergence angles of the beam, with spacing constraints typically dictating this distance. To achieve equal power splitting of the beams at the Wollaston prism, WP_1, the input beam must be either linearly polarized at 45° to the splitting axis of Wollaston prism or be circularly polarized. Since most laser beams are already strongly linearly polarized, a half wave-plate, HWP, can be used to rotate the polarization state to 45° or a quarter-wave plate can be used to convert to circularly polarized light. If other than x-gradients are desired, the Wollaston prism and half-wave plate must be rotated together; if using a quarter-wave plate, then only the Wollaston prism must be rotated. Once the beam is conditioned correctly, the Wollaston prism splits the beam by small angle, ϵ, typically on the order of 1-10 arcmin [18]. The two beams, now mutually orthogonal to one another, are focused by a field lens, F_1, located one focal length, f_{F_1}, away from the Wollaston prism. This distance, S_2, is equal to f_{F_1} to ensure the beams travel parallel through the test section. After the first field lens, the beams travel to a point in the center of the test section separated by a small distance, Δx, otherwise known as the beam pair spacing. This distance is given by:

$$\Delta x = 2 f_{F_1} \tan\left(\frac{\epsilon}{2}\right) \tag{2.1}$$

After reaching the focal point of the system, the beams expand to the catch side of the system where an identical field lens, F_2, refocuses the beams onto an identical Wollaston prism, WP_2, where the beams are recombined. Once combined, the two beams pass through an additional polarizer, P, aligned with the input polarization state to permit optical interference. A photodetector, PD, is placed after the polarizer that outputs a voltage proportional to the fluctuating intensity of the interfering beams. This intensity of the laser beam is related to phase difference as will be subsequently shown in Section 2.2.

To design an FLDI system, distances between optical components and lens focal lengths must be considered. The sensitivity of FLDI is a function of laser wavelength, λ_0, beam radius at the focus, ω_0, and beam separation distance, Δx as shown in the Introduction by Equation 1.2. While Δx is quantified by Equation 2.1, ω_0 is much harder to determine since Gaussian beams vary non-linearly with position between optics. Equation 2.2 shows how beam radii are a function of ω_0, λ_0, and position along the optical axis, z. For lasers with high beam quality such as HeNe's, this expression remains unchanged; however, for beams which poorly approximate a Gaussian beam, the M^2 value for the laser should be determined experimentally and applied to the λ_0 term of the expression. The M^2 simply accounts for how much the beam diverges from a Gaussian profile. In practice, Δx and ω_0 can both be measured by a beam profiler to confirm design choices. To model FLDI beam propagation, ray-transfer matrices can be used to identify the position of focus and beam radius at the focus. While first implemented by Gragston [15] using the Thin Lens Equation (Equation 2.3), a more thorough use of ray-transfer matrices utilizes complex beam parameters to model Gaussian beam propagation as shown by Neet *et al* [19] - both of which are implemented in this thesis.

$$\omega(z)^2 = \omega_0^2 \left[1 + \left(\frac{\lambda_0 \, z}{\pi \, \omega_0^2} \right)^2 \right] \tag{2.2}$$

$$\frac{1}{S_2 + f_D} + \frac{1}{S_3} = \frac{1}{f_{F_1}} \tag{2.3}$$

Since FLDI sensitivity is a function of λ_0, ω_0, and Δx, the design of the system is a careful optimization of the distances between lenses and their focal lengths. The optimization is a function of the following parameters: $\{S_1, S_2, S_3, f_D, f_{F_1}\}$ which affect ω_0 and Δx. Further, careful selection of these quantities is imperative to not to exceed apertures of the lenses while also balancing beam expansion and the lens $F\#'s$ so that optical aberration does not significantly alter the beam waist at the focus. The $F\#$ is the ratio between the lens focal length and the beam diameter at the lens.

2.1.1 Voltage to Phase Difference

The phase difference of the interferometer can be expressed by the superposition of Jones vectors from each beam. The Jones vectors and hence electric fields can be converted to laser beam intensity as was shown by Schmidt and Shepherd [9] who derived the equations from Born and Wolf [20]. The reader is directed to Fulghum's dissertation [11] for more detail on Jones vectors. From this, the intensity of light incident on the photodetector, E_{PD}, is shown to be a function of phase difference, $\Delta\phi$, and the individual intensities of each beam, E_1 and E_2 respectively, given by:

$$E_{PD} = E_1 + E_2 + 2\sqrt{E_1 E_2}\cos(\Delta\phi) \tag{2.4}$$

Since both beams are split equally by the Wollaston prism, it is assumed that $E_1 = E_2 = E_b$ where E_b is the intensity of a single beam. The equation can then be g:

$$E_{PD} = 2E_b[1 + \cos(\Delta\phi)] \tag{2.5}$$

As shown by Benitez *et al* [18], perfect contrast between the interfering beams is unlikely due to laser and optical imperfections; thus a constant intensity, $E_{\min}$, is added to the equation. Further, a constant phase shift of $\Delta\phi_0$ is typically added to account for translating the Wollaston prism by the user across the beam path. The resultant equation is given by:

$$E_{PD} = 2E_b[1 + \cos(\Delta\phi + \Delta\phi_0)] + E_{\min} \tag{2.6}$$

If $\Delta\phi_0$ is set at $\pi/2$ so that the intensity is placed at the middle of the interference fringe pattern, then the cosine term can be rewritten with a sine term. Further simplification with $E_{max} = 4E_b + E_{min}$ yields Equation 2.7. This simplification comes from foiling Equation 2.6 and solving for E_{max} when $\cos(\Delta\phi) = 1$.

$$E_{PD} = \frac{1}{2}[E_{\max} + E_{\min} + (E_{\max} - E_{\min})\sin(\Delta\phi)] \tag{2.7}$$

From this equation, voltage can be related to intensity incident on the photodetector face by $E_{PD} = VH_{PD}$, where H_{PD} is a transfer function that accounts for the photodetector response time and resistive load. This value is typically determined using a pulsed LED to test the photodetector response; but most assume this value to be 1. Using this, Equation 2.7 can be rewritten as:

$$V = \frac{H_{PD}}{2}[V_{\max} + V_{\min} + (V_{\max} - V_{\min})\sin(\Delta\phi)] \tag{2.8}$$

Inverting Equation 2.8 gives the phase difference of FLDI as a function of the output voltage. The minimum and maximum voltages in the equation correspond to the dark and light fringes of the interference pattern. Shown in Figure 2.2, the most ideal response of the interferometer is when the voltage is set near the linear portion of the interference fringe. This avoid phase wrapping that occurs near the edges of the fringes. Recalling that the cosine term in Equation 2.6 was swapped with sine, the middle of the fringe corresponds to a $\Delta\phi_0 = \pi/2$. This corresponds to a voltage of roughly $V_0 = (V_{\max} + V_{\min})/2$. The equation for phase difference is given as:

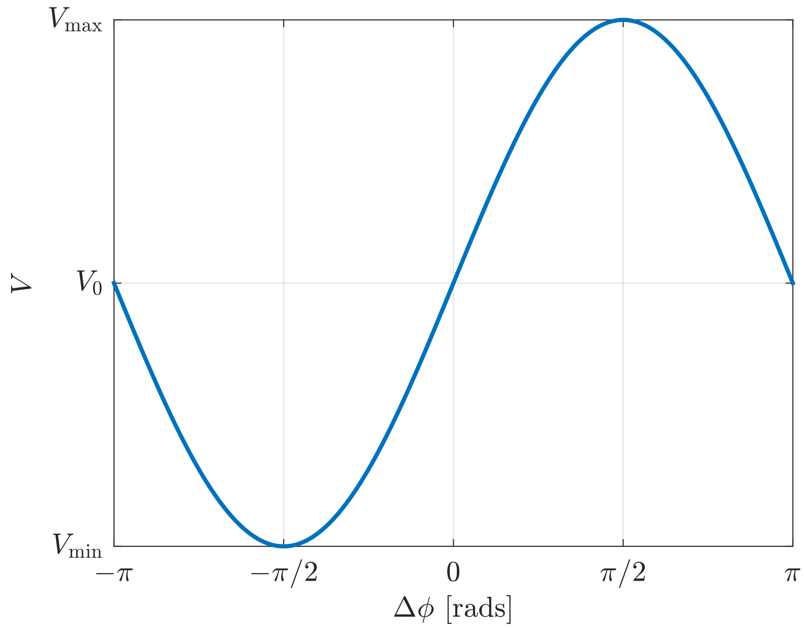

Figure 2.2: Expected output of photodetector showing the sinusoidal relationship between $\Delta\phi$ and V. Note the middle of the sinusoid corresponds to the middle of the fringe at V_0 and $\Delta\phi_0 = \pi/2$. The ideal alignment of the interferometer is when the Wollaston prism is translated to achieve a V_0 in the middle of the sinusoid to reduce phase wrapping from the edges of the constructive and destructive interference fringes.

$$\Delta\phi = \sin^{-1}\left(\frac{\frac{2V}{H_{PD}} - V_{\max} - V_{\min}}{V_{\max} - V_{\min}}\right) \tag{2.9}$$

2.1.2 Phase Difference to Index of Refraction

The phase difference of the FLDI signal can be related to index of refraction by Equation 2.10. This equation was adapted from Cerruzi's dissertation [21] who adapted the equation from Schmidt and Shepherd [9]. In the equation, S and D are the positions of the laser and photodetector respectively, and s_1 and s_2 are the axes along which each beam travels. $n(\boldsymbol{x})$ is the index of refraction field as a function of the position vector, $\boldsymbol{x}$, in three dimensions. E_0

is the baseline intensity on the photodetector with no phase difference, and ξ and η represent the directions of integration on the detector face.

$$\Delta\phi = \frac{2\pi}{\lambda_0} \iint_D E_0 \left[\int_S^D n(\boldsymbol{x}_1) ds_1 - \int_S^D n(\boldsymbol{x}_2) ds_2 \right] d\xi \, d\eta \tag{2.10}$$

Using the Gladstone-Dale relationship, Equation 2.10 can be rewritten to express density as shown in Equation 2.12.

$$n = K\rho + 1 \tag{2.11}$$

$$\Delta\phi = \frac{2\pi K}{\lambda_0} \iint_D E_0 \left[\int_S^D \rho(\boldsymbol{x}_1) ds_1 - \int_S^D \rho(\boldsymbol{x}_2) ds_2 \right] d\xi \, d\eta \tag{2.12}$$

Equation 2.10 shows that phase difference can be solved for when a index of refraction field is fully defined. However, this equation is not invertible, therefore simplifying assumptions must be made of the index of refraction field in order to resolve index of refraction from phase differences. With current theory, transfer functions are used to model the form of the index of refraction disturbances. Many authors have provided methods of inverting Equation 2.10, but Lawson [14] provides the most up to date version of utilizing transfer functions to convert the Power Spectral Density, PSD, of phase difference to index of refraction fluctuations. Converting phase difference to index of refraction is beyond the scope of this work; instead, transfer functions will be used to examine the wavenumber sensitivity of FLDI.

2.2 Analytical Transfer Functions

2.2.1 FLDI Sensitivity

The method for deriving the transfer functions described in the following section has been written in detail by many authors. The reader is referred to the cumulative paper on FLDI from Benitez *et al* [18] that shows the general process and where to look for specific variants. In general, transfer functions are developed by either using the derivative of the phase difference gradient or by reducing the integral of Equation 2.10 analytically. In this thesis, forms of the transfer functions developed by Ceruzzi [12] and Lawson [14] will be used. The basic form of the FLDI transfers functions are described by two equations, $H_{\Delta x}$ and H_ω; with a combined transfer function of $H = H_{\Delta x}H_\omega$. Each component of this equation is shown in Equation 2.13 and Equation 2.14 respectively where $H_{\Delta x}$ represents the response due to the beam spacing between the two beams and H_ω represents the response due to the focusing of the beams. The combined transfer function succinctly describes the response of FLDI as a function of the x-disturbance wavenumber, k_x, beam spacing, Δ_x, and beam radius along along the optical axis, $\omega(z)$.

$$H_{\Delta x}(k_x) = \sin\left(\frac{k_x \Delta x}{2}\right) \tag{2.13}$$

$$H_\omega(k_x, z) = \exp\left(-\frac{k_x^2 \omega(z)^2}{8}\right) \tag{2.14}$$

In the following forms of the transfer functions, Equations 2.13 and 2.14, will be used following the process outlined by Ceruzzi [12] and Lawson [14]. These transfer functions differ slightly from those reported by Schmidt and Shepherd [9] and earlier authors. In these previous works, the transfer functions were derived defining H as a ratio between the maximum of $\Delta\phi/\Delta x$ and its derivative which produces a normalized system transfer function which is equivalent but not required to express the response of the system. Here, H_{Δ_x} and H_ω are derived by analytically reducing the integrand of Equation 2.10. Further, H_ω, can vary along the optical axis and is not integrated within the test section bounds. This is a major assumption which results in this transfer function not representing the real signal - this will be accounted for with integration in the rest of this section.

Following this, Equation 2.14 can be rewritten using the equation for Gaussian beam radius, Equation 2.2, giving:

$$H_\omega(k_x, z) = \exp\left(-\frac{k_x^2\omega_0^2}{8} - \frac{k_x^2\lambda_0^2 z^2}{8\pi^2\omega_0^2}\right) \tag{2.15}$$

The combined transfer function then becomes:

$$H(k_x, z) = \sin\left(\frac{k_x \Delta x}{2}\right)\exp\left(-\frac{k_x^2\omega_0^2}{8} - \frac{k_x^2\lambda_0^2 z^2}{8\pi^2\omega_0^2}\right) \tag{2.16}$$

Equation 2.16 describes the wavenumber sensitivity of FLDI, assuming sinusoidal plane wave disturbances in the x-direction. The combined transfer function describes the response of FLDI as a function of k_x and z with Δx, laser wavelength, λ_0, and beam radius at the focus, ω_0, being constants set by the FLDI configuration. This form of the combined transfer function is represented by Figure 2.3 which allows the comparison of FLDI sensitivity across varying configurations. Figure 2.3 and Equation 2.13 shows that FLDI is sensitive to a narrow band of wavenumbers centered around a wavenumber of $k_{x,\,sensitive} = \pi/\Delta x$. Specifically, Figure 2.3 shows that sensitivity decreases for both smaller and higher wavenumbers about the most sensitive wavenumber, and aliasing occurs at wavenumbers of $k_x = \frac{2\pi n}{\Delta x}$ for any positive integer n. Noticeably, low wavenumbers have a much higher probability of contributing to the signal away from the focus. Since FLDI's signal attenuation near the focus is due to the local beam diameter being smaller than large disturbance wavelengths (low wavenumbers), as the beams expand away from the focus, large disturbance wavelengths greater than the beam diameter are subsequently resolved. However as shown by Fulghum [11], these low wavenumbers, although present, are filtered due to producing weaker gradients for a fixed amplitude compared to high wavenumber disturbances.

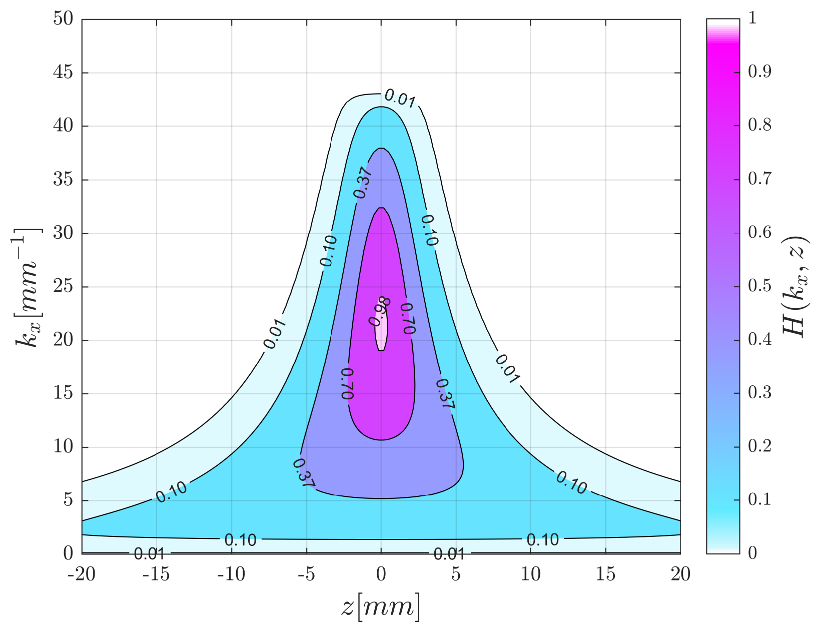

Figure 2.3: Example non-spatially integrated combined transfer function results for a typical FLDI configuration used to analyze the analytical resolution of the instrument. Note that wavenumbers around $k_{x,\,sensitive} = \pi/\Delta x$ are uniformly attenuated by Δx while low wavenumbers are filtered due to weak gradients but are still present. Aliasing occurs at wavenumbers past $k_{x,\,sensitive} = \pi/\Delta x$. This plot shows wavenumbers corresponding to disturbance wavelengths between $0 - 20\,m$.

Spatially, the resolution of FLDI around the focus, in X_{SR}, Y_{SR}, and Z_{SR}, can be described by geometric parameters. Adapted from Benitez *et al* [18], $X_{SR} = \Delta x$ and $Y_{SR} = 2\omega_0$. Although more difficult to measure, Z_{SR} can be determined by the position away from the focus in which the transfer function magnitude drops to $1/e$ of its maximum. Otherwise put as $Z_{SR} = 2z_{1/e}$. First developed by Cerruzi [22], this equation is given in Equation 2.17. This equation shows that Z_{SR} is the most limiting value for spatial resolution since it depends on the disturbance wavenumber; hence FLDI provides a "point-like" measurement, but does not have the same resolution in each direction. In much of the results of this work, Z_{SR} will be represented in terms of the instruments most sensitive wavenumber or $Z_{SR,\,sensitive}$, which gives a good comparison between FLDI configurations when trying to match which wavenumbers the system is most sensitive to and the resolution at this value. The equation for $Z_{SR,\,sensitive}$ is given by Equation 2.18

$$Z_{SR} = \frac{4\pi^2\sqrt{2}\omega_0}{\pi\lambda_0 k_x} \tag{2.17}$$

$$Z_{SR,\,sensitive} = \frac{2\pi^2\sqrt{2}\omega_0\Delta x}{\pi\lambda_0 k_x} \tag{2.18}$$

While Equation 2.15 represents the transfer function with respect to z and k_x, it is useful to identify the transfer function response integrated across z as this is what the instrument will truly measure. Equation 2.16 is analytically integrated over the bounds of a disturbance; which when considering the instrument is probing a wind tunnel, the bounds of integration is the tunnel width, d_t. This method was pioneered by Schmidt and Shepherd [9] and also adapted in Lawson's dissertation [14]. Using this method, the entire frequency response of the real instrument can be inspected. Comparing the response of the real instrument to an idealized instrument illuminates how the real instrument resolves low wavenumbers away from the focus. These low wavenumber disturbances, however, are assumed to be filtered due to having weaker gradients than compared to high wavenumber disturbances. An example showing the difference in response between the real instrument and the idealized instrument is given in Figure 2.4. The figure shows the contribution from each component of the transfer function: $H_{\Delta x}$ and H_{ω}. Note the broadband sensitivity to low wavenumbers that are assumed to filter out and the aliasing that occurs after $k_{x,\, sensitive} = \pi/\Delta x$. The following equation showing the integrated transfer function was adapted from Lawson's dissertation [14].

$$H(k_x) = \frac{4\sqrt{2}\pi^{\frac{3}{2}}\omega_0}{k_x\lambda_0} \sin\left(\frac{k_x\Delta x}{2}\right) \exp\left(-\frac{k_x^2\omega_0^2}{8}\right) \operatorname{erf}\left(\frac{k_x d_t \lambda_0}{2\sqrt{2}\pi\omega_0}\right) \tag{2.19}$$

$$\Delta\phi = n * H(k_x) \tag{2.20}$$

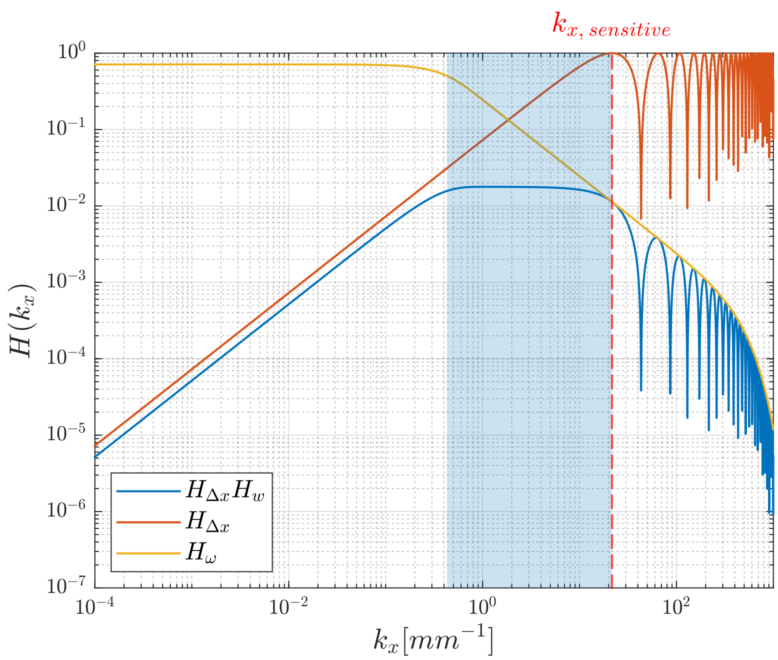

Figure 2.4: Example result of the integrated transfer function for a typical FLDI configuration - split between each transfer function component of H. Note the peak sensitive band of the interferometer beneath $k_{x,\, sensitive}$ which is due to small beam diameters away from the focus permitting large wavelength disturbances to be resolved.

From the preceding discussion: analyzing the combined transfer function plots (Figure 2.3 and 2.4), $k_{x,\,sensitive}$, and $Z_{SR,\,sensitive}$ for various FLDI configurations allows the comparison of the instruments spatial and temporal sensitivity. In section 2.3.1 of this chapter, these metrics will be used with scaling to identify how to match FLDI sensitivity across flows and facilities of various size.

2.2.2 Applied to Jets in High-Speed Cross-Flow

Probing jets in high-speed cross-flow with FLDI has not been considered much in literature. In most cases, FLDI has been applied to high-speed freestream turbulence where the model for sinusoidal plane wave disturbances in the x-direction can be applied. Since jets in cross-flow are at least two-dimensional in the xy-plane, Lawson's transfer functions [14] must be used which account for index of refraction disturbances in multiple directions. As shown by Lawson, the only term in the transfer function equation modified when accounting for multiple directions is the wavenumber. From this, the combined transfer function for FLDI accounting for sinusoidal plane-wave disturbances in the xy-plane is given by the following equation:

$$H(k_x, k_z, z) = \sin\left(\frac{k_x \Delta x}{2}\right) \exp\left(-\frac{[k_x^2 + k_y^2]\omega_0^2}{8} - \frac{[k_x^2 + k_y^2]\lambda_0^2 z^2}{8\pi^2\omega_0^2}\right) \tag{2.21}$$

Equation 2.21 can be reduced using wavenumber magnitude with $k^2 = k_x^2 + k_y^2$. Assuming disturbances in the xy-plane are oriented at some degree, α, the equation can be further reduced by substituting the wavenumber component in the x-direction, $k_x = k\cos(\alpha)$, into the $H_{\Delta x}$ term. Equation 2.21 then becomes Equation 2.22. Compared to Equation 2.16, this equation scales $k_{x,\,sensitive}$ by $\cos(\alpha)^{-1}$.

$$H(k,z) = \sin\left(\frac{k\cos(\alpha)\Delta x}{2}\right)\exp\left(-\frac{k^2\omega_0^2}{8} - \frac{k^2\lambda_0^2 z^2}{8\pi^2\omega_0^2}\right) \tag{2.22}$$

Although the FLDI transfer functions have been developed using disturbance wavenumbers, it is often more useful to work in terms of frequencies. This is because results are typically analyzed in frequency space with PSD plots. Wavenumber can be converted to frequency using a velocity. In this thesis, the jet velocity, U_j, is used; however, it is more commonplace to see the convective freestream velocity used. The conversion is given by the Equation 2.23.

$$f = \frac{kU_j}{2\pi} \tag{2.23}$$

Substituting Equation 2.23 into Equation 2.22 yields Equation 2.24, given below:

$$H(f,z) = \sin\left(\frac{f\cos(\alpha)\pi\Delta x}{U_j}\right)\exp\left(-\frac{f^2\pi^2\omega_0^2}{2U_j^2} - \frac{f^2\lambda_0^2 z^2}{2U_j^2\omega_0^2}\right) \tag{2.24}$$

In the literature for jets in cross-flow, the Strouhal number is used to non-dimensionalize a frequency. For jets in cross-flow, the convention is to use the jet size, d_j, and jet velocity to non-dimensionalize frequency as shown in Miller *et al* [1] and given by Equation 2.25. The Strouhal number is used to quantify the unsteady frequencies of the flow with respect to the velocity and physical size of the jet.

$$St = \frac{fd_j}{U_j} \tag{2.25}$$

Substituting Strouhal number into Equation 2.24 yields Equation 2.26, shown here:

$$H(St, z) = \sin\left(\frac{St\cos(\alpha)\pi\Delta x}{d_j}\right)\exp\left(-\frac{St^2\pi^2\omega_0^2}{2d_j^2} - \frac{St^2\lambda_0^2 z^2}{2d_j^2\omega_0^2}\right) \tag{2.26}$$

The preceding transfer function equations applied to jets in cross-flow can be integrated along z to show the resolution of the real instrument along the beam path. This is accomplished using the method discussed at the end of Section 2.2.1 and described by Lawson's dissertation [14]. Presented here, the form of Equation 2.19 adapted for jets in cross-flow is given by Equation 2.26. Similarly, the sensitive Strouhal number can be converted from wavenumber and is give be $St_{sensitive} = \frac{d_j}{2\Delta x}$.

$$H(St) = \frac{2\sqrt{2\pi}\omega_0 d_j}{St\lambda_0}\sin\left(\frac{St\cos(\alpha)\pi\Delta x}{d_j}\right)\exp\left(-\frac{St^2\pi^2\omega_0^2}{2d_j^2}\right)\operatorname{erf}\left(\frac{Std_t\lambda_0}{\omega_0 d_j\sqrt{2}}\right) \tag{2.27}$$

Equation 2.27 is incredibly useful because when compared to the non-spatially integrated transfer function, Equation 2.26, this equation shows that FLDI is actually sensitive to much lower Strouhal numbers than what would be expected from just $St_{sensitive}$. This as an important result because it quantifies how much the instrument is sensitive to low Strouhal numbers across the beam path, which is a result of the large beam diameters away from the focus. This equation is visualized using wavenumber in Figure 2.4 which shows this characteristic.

2.3 Theoretical Analysis

One objective of this thesis is to implement the FLDI transfer functions for three distinct optical configurations, matching the model scale of wind tunnels with diameters ranging from 1 ft to 4 ft. To evaluate how variations in the optical components affect sensitivity across these tunnels, FLDI ray-tracing and the non-spatially integrated transfer function (Equation 2.16) were both implemented in MATLAB.

Three different tunnel scales were simulated ranging from from 1 ft to 4 ft. To match scaling between FLDI configurations, the model or jet of interest is assumed to be approximately $1/6^{th}$ the size of the tunnel diameter. Table 2.1 shows the tunnel diameters and model scale of interest used for simulating each wind tunnel. In the table, the tunnel diameter is represented by d_t and the model scale is represented by d_s. d_s is used as the scaling parameter in all transfer function equations throughout the rest of this chapter.

Table 2.1: Physical dimensions of tunnel diameters, d_t and model scale, d_s, used to define tunnel size scaling of FLDI transfer functions. Three scales of facilities are defined, Tunnel 1, Tunnel 2, and Tunnel 3, shown here in increasing order.

Parameter	**Tunnel 1**	**Tunnel 2**	**Tunnel 3**	**Units**
$\boldsymbol{d_t}$	0.3	1.6	4	ft
$\boldsymbol{d_s}$	14.8	83.3	203.2	mm

2.3.1 FLDI Sensitivity Scaling

Following the nomenclature presented in Section 2.1, three optical configurations were designed to match FLDI sensitivity between the three sizes of facility. For all of the configurations, a laser wavelength was specified at $\lambda_0 = 632.8\,nm$ and the input beam diameter was set at $0.7\,mm$ which is representative of typical HeNe lasers. To accommodate increasing scale, the focal length of the diverging lens, f_D, was decreased while the focal length of the field lens, f_{F_1}, distance between the diverging lens and field lens, S_2, and the Wollaston prism splitting angles, ϵ, were increased. Figure 2.5 shows how manipulating these optical design choices affects the physical footprint of the system. Note that the physical footprint of the system for Tunnel 2 and Tunnel 3 does not change much, since the Wollaston prism was primarily the only optic changed. The blue and orange rays represent the two mutually orthogonal polarization states due to the splitting at the Wollaston prism. Table 2.2 shows the key optical design choices and the resultant spatial resolution and sensitive wavenumbers for each configuration. The last two columns of this table represent the scaled quantities for the spatial resolution and sensitive wavenumber. All cells highlighted in green show matched quantities between wind tunnels.

Table 2.2: Results of FLDI sensitivity scaling between three tunnel diameters. The first five columns represent the input parameters for each FLDI configuration while the remaining six represent the unscaled and scaled outputs. Cells are highlighted with green to show matched sensitivity results between each tunnel FLDI configuration.

Parameter	**Tunnel 1**	**Tunnel 2**	**Tunnel 3**	**Units**
$\boldsymbol{d_s}$	14.8	83.3	203.2	mm
$\boldsymbol{f_D}$	25	–6	5	mm
$\boldsymbol{f_{F_1}}$	35	200	200	mm
$\boldsymbol{S_2}$	142	305	300	mm
$\boldsymbol{\epsilon}$	2	2	5	arcmin
$\boldsymbol{\omega_0}$	5.04	4.95	4.86	μm
$\boldsymbol{\Delta x}$	20.36	116.36	290.89	μm
$\boldsymbol{Z_{SR,\ sensitive}}$	0.90	5.05	12.39	mm
$\boldsymbol{k_{x,\ sensitive}}$	154.29	27.00	10.80	mm^{-1}
$\boldsymbol{Z_{SR,\ sensitive}/d_s}$	0.061	0.061	0.061	–
$\boldsymbol{k_{x,\ sensitive}\ d_s}$	2286.00	2250.00	2194.56	–

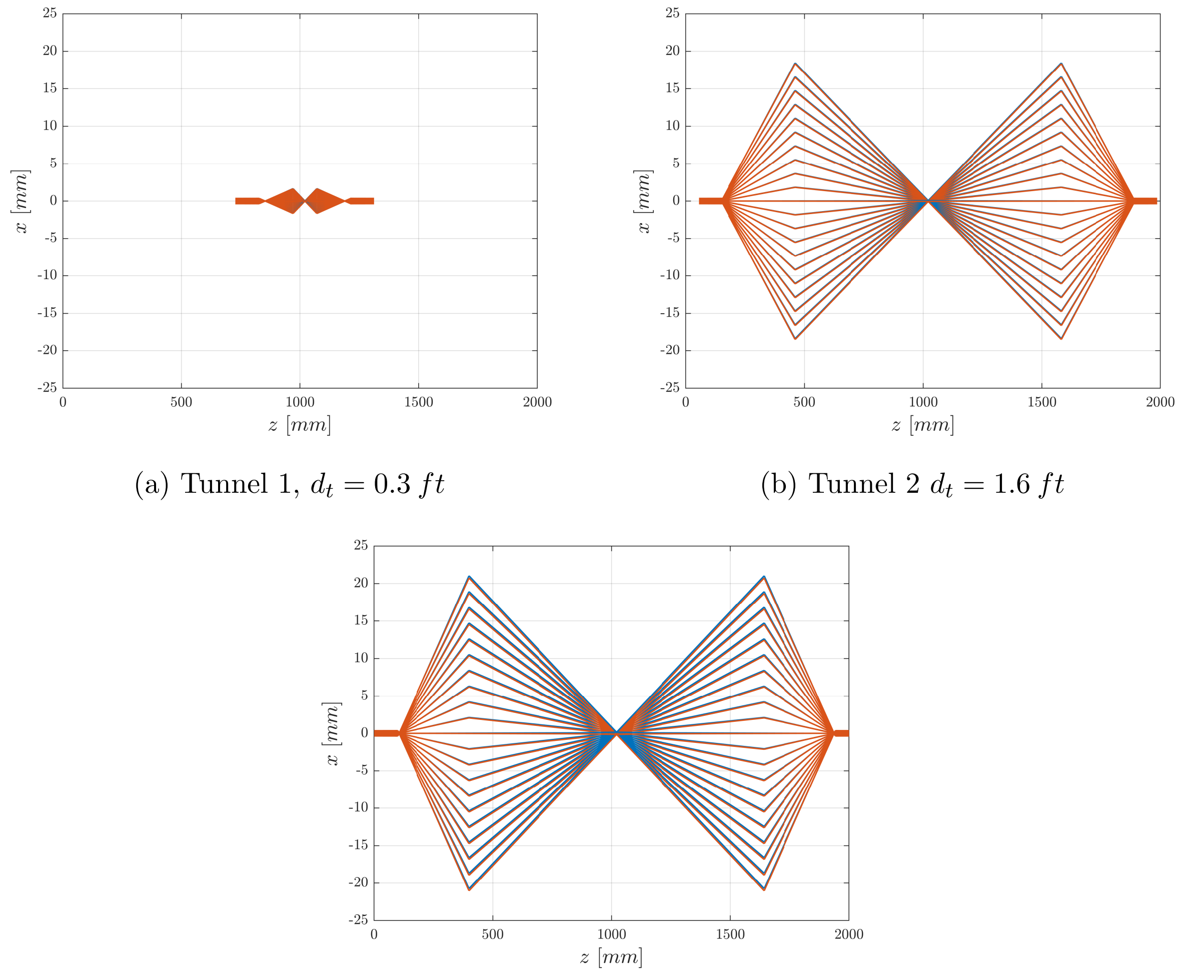

(a) Tunnel 1, $d_t = 0.3\ ft$

(b) Tunnel 2 $d_t = 1.6\ ft$

(c) Tunnel 3 $d_t = 4\ ft$

Figure 2.5: Gaussian ray-tracing plots for each wind tunnel FLDI configuration. Organized by increasing tunnel diameter. Note the physical footprint of each configuration changes based on tunnel dimensions.

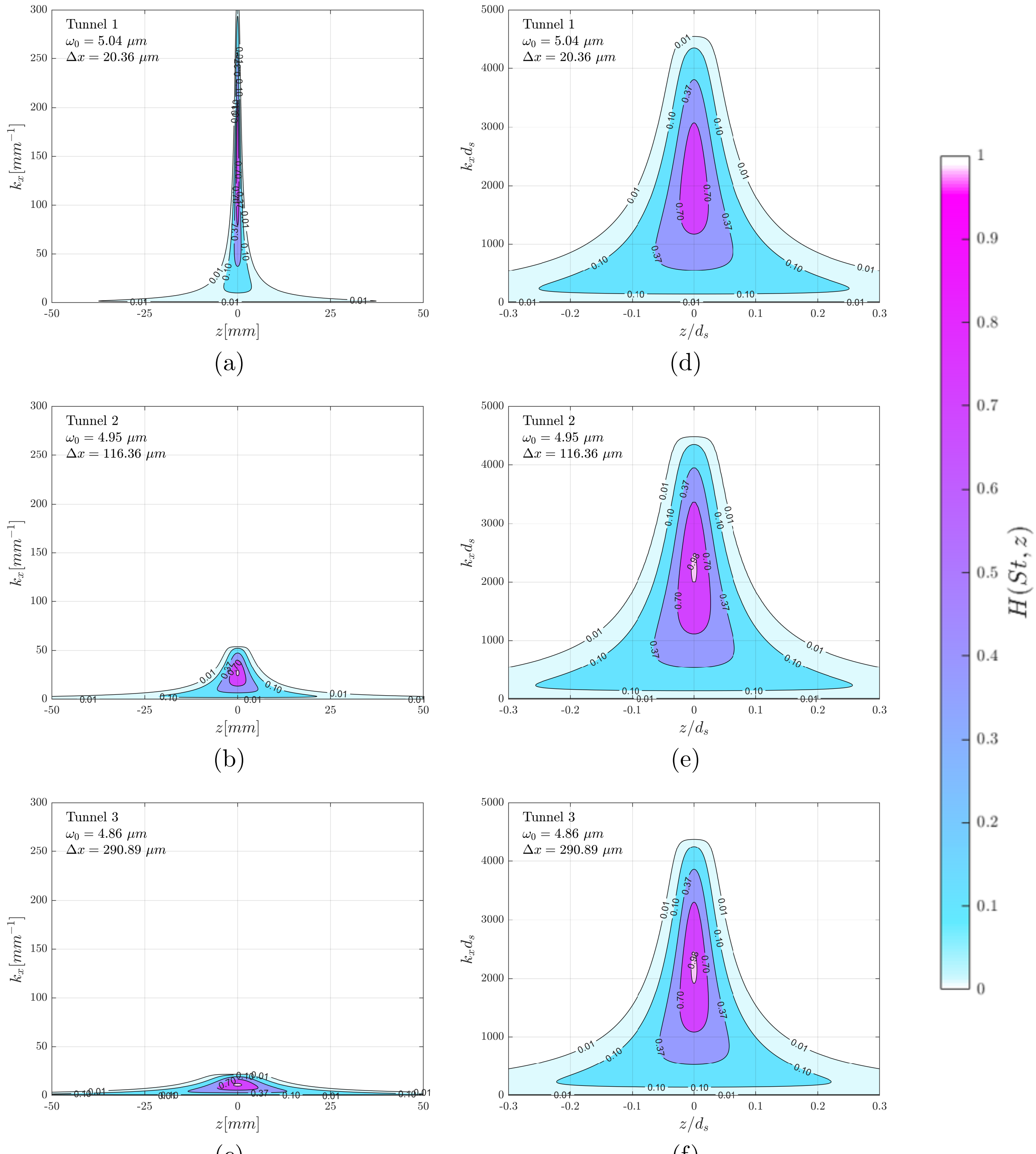

Figure 2.6: Non-spatially integrated combined transfer functions with and without scaling applied. Moving down each column corresponds to changing tunnel diameters while moving across each row correspond to dimensional and non-dimensional FLDI sensitivity.

The results of this analysis are presented in Figure 2.6. Each column represents the unscaled and scaled response of FLDI respectively. The left column, Figures 2.6a - 2.6c, summarizes the dimensional sensitivity of each configuration; whereas the right column, Figures 2.6d - 2.6f, show the non-dimensional sensitivity relative to the size of the tunnel, suggesting that the relative sensitivity is very similar between each of the three cases. Using the integrated transfer function, shown in Figure 2.7, the scaled response for each configuration show matched profiles which means each is sensitive to the same band of wavenumbers. However, the magnitudes of each are displaced, with increasing d_t corresponding to an increase in transfer function magnitude. This suggests that sensitivity does not quite match response between tunnels and that tunnel diameter does plays a role - this makes sense by Equation 2.19 in which the transfer function is dependent on the bounds of integration, d_t.

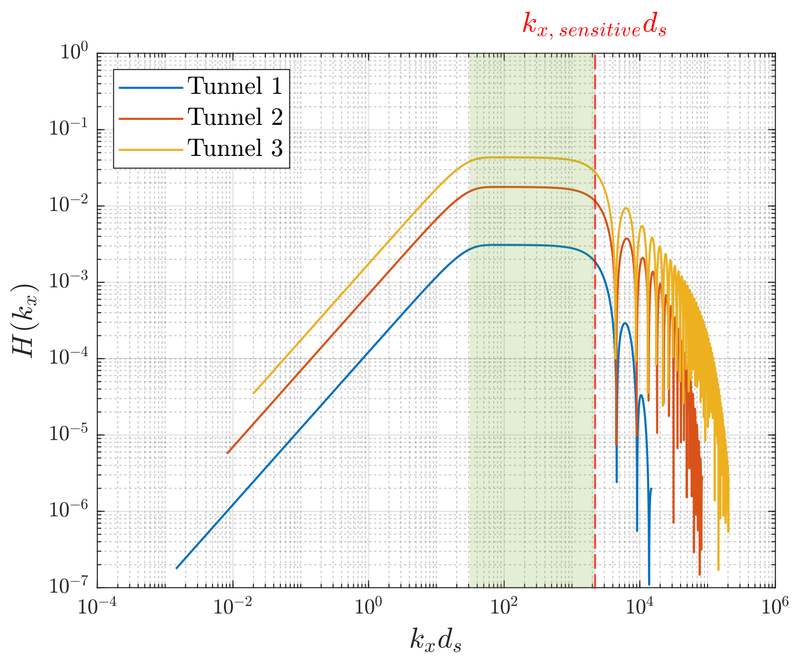

Figure 2.7: Integrated combined transfer function results for scaled FLDI configurations. Note the matched peak sensitive band of the instrument beneath $k_{x,\,sensitive}$ for each configuration. Noticeably, the magnitude of the transfer function scales with tunnel diameter.

In general, scaling is incredibly important when considering how to apply this diagnostic to different sizes of wind tunnels and flows. For one-off experiments in a single tunnel, scaling is not integral to the design choices of FLDI - instead FLDI should be tuned to probe specific wavenumbers that would be expected within a desired spatial resolution. However, if results are to be compared quantitatively between facilities, the physical size should be accounted for. Sensitivity is matched through careful selection of the FLDI optics and distances between lenses. The following design tips and tradeoffs are useful when creating an FLDI system:

The wavenumber sensitivity of the instrument is set by several parameters: mainly Δx and $\omega(z)$ which are both determined by choice of optics. To probe low wavenumber disturbances, Δx should be increased by raising ϵ or f_{F_1} (Equation 2.1). Δx is typically kept small to ensure the instrument is approximating the gradient of index of refraction. A tradeoff exists between increasing Δx to probe low wavenumbers and degrading the index of refraction gradient approximation. However, if increasing Δx to accommodate an increase in tunnel size, then the gradient approximation will likely hold since disturbances will also scale similarly. Increasing Δx will seemingly make the peak sensitive band of the integrated transfer function plot in Figure 2.7 more narrow, but the entire magnitude will increase which shows that increasing Δx successfully probes lower wavenumbers. Varying f_{F_1}, f_D, and S_2 all change ω_0, $\omega(z)$, and the physical size of the system. In general, decreasing f_{F_1}, f_D, and S_2 all decrease ω_0 due to increasing the beam divergence angle. Beams with a large divergence angle and small ω_0 attenuate high wavenumbers rapidly away from the focus due to their small beam diameter - this has the effect of increasing the roll-off in Figure 2.7. To shift the left boundary of the peak sensitive band in Figure 2.7, both Δx should be increased and the beam diameter at the field lens should also be increased. Having a large beam diameter at the field lens ensures the roll-off point is shifted to lower wavenumbers, but this will also reduce the magnitude of the transfer function. Reference Figure 2.4 to show how changing

$H_{\Delta x}$ and H_ω can each change the response of the integrated transfer function. In general, there are tradeoffs with all of these design choices, but they will all shift the sensitivity to lower wavenumbers.

For increasing tunnel size, Δx should be increased by the same scale factor and f_{F_1}, f_D, and S_2 should be adjusted together to keep a similar ω_0 between configurations. Ray-tracing should be utilized throughout this process to ensure real focal points are achieved, lens apertures are not exceeded, and to ensure the field lenses are beyond the width of the tunnel. The beam waist should be kept relatively like ensure the scaled spatial resolution of each configuration at their respective sensitive wavenumbers are the same. Recall that spatial resolution is different in each axis, all of which are either a function of Δx or ω_0. Keeping ω_0 constant while scaling k_x will ensure that Z_{SR} and Y_{SR} are matched appropriately. X_{SR} will also scale correctly if divided by d_s.

The remainder of this thesis utilizes FLDI to probe a single wind tunnel, precluding comparisons of scaled FLDI sensitivity. Because of this, explorations of FLDI sensitivity and transfer function fidelity are performed by exploring the impact of resolution and sensitivity within the same facility. By showing that sensitivity changes between configurations, the importance of scaling can be revealed. Later in this thesis, two FLDI configurations will be applied to the same test case to address changing sensitivity.

REFERENCES

[1] Miller, W. A., Medwell, P. R., Doolan, C. J., and Kim, M., "Transient interaction between a reaction control jet and a hypersonic crossflow," *Physics of Fluids*, Vol. 30, No. 4, 04 2018, pp. 046102.

[2] Gillespie, G. I., Ceruzzi, A. P., and Laurence, S. J., "A multi-point focused laser differential interferometer for characterizing freestream disturbances in hypersonic wind tunnels," *Experiments in Fluids*, Vol. 63, 2022, pp. 180.

[3] Mahesh, K., "The Interaction of Jets with Crossflow," *Annual Review of Fluid Mechanics*, Vol. 45, No. 1, Jan. 2013, pp. 379–407.

[4] Viti, V., Neel, R., and Schetz, J. A., "Detailed Flow Physics of the Supersonic Jet Interaction Flow Field," *Physics of Fluids*, Vol. 21, No. 4, 2009, pp. 046101.

[5] Ben-Yakar, A., *Experimental Investigation of Mixing and Ignition of Transverse Jets in Supersonic Crossflows*, Ph.d. thesis, Stanford University, Stanford, CA, 2000, Department of Mechanical Engineering.

[6] Ben-Yakar, A., Mungal, M. G., and Hanson, R. K., "Time Evolution and Mixing Characteristics of Hydrogen and Ethylene Transverse Jets in Supersonic Crossflows," *Physics of Fluids*, Vol. 18, No. 2, Feb. 2006, pp. 026101.

[7] Smeets, G. and George, A., "Gas-Dynamic Investigations in a Shock Tube using a Highly Sensitive Interferometer," Tech. Rep. 14/71, Institut Franco-Allemand de Recherches de Saint-Louis, 1971, Translation by Andreas R. Goetz, Purdue University, 1996; corrected by G. Smeets.

[8] Smeets, G. and George, A., "Laser-Differential Interferometer Applications in Gas Dynamics," Technical Report 28/73, Institut Franco-Allemand de Recherches de Saint-Louis, 1973, English translation by Andreas R. Goetz, Purdue University, 1996; corrected by G. Smeets.

[9] Schmidt, B. E. and Shepherd, J. E., "Analysis of focused laser differential interferometry," *Applied Optics*, Vol. 54, 10 2015, pp. 8459.

[10] Parziale, N., *Slender-Body Hypervelocity Boundary-Layer Instability*, Ph.D. thesis, California Institute of Technology, Pasadena, CA, May 2013.

[11] Fulghum, M. R., *Turbulence Measurements in High-Speed Wind Tunnels Using Focusing Laser Differential Interferometry*, Ph.d. dissertation, Pennsylvania State University, University Park, PA, Aug. 22 2014.

[12] Ceruzzi, A. P., *Development of Two-Point Focused Laser Differential Interferometry for Applications in High-Speed Wind Tunnels*, Ph.D. thesis, University of Maryland, College Park, 2022.

[13] Lawson, J. M., Neet, M. C., Grossman, I. J., and Austin, J. M., "Static and dynamic characterization of a focused laser differential interferometer," *Experiments in Fluids*, Vol. 61, 8 2020.

[14] Lawson, J. M., *Focused Laser Differential Interferometry*, Ph.D. thesis, California Institute of Technology, Pasadena, CA, 2021.

[15] Gragston, M., Price, T. J., Davenport, K., Schmisseur, J. D., and Zhang, Z., "An m × n FLDI array for single-shot, multipoint disturbance measurements in high-speed flows," *AIAA Scitech 2021 Forum*, American Institute of Aeronautics and Astronautics, 2021, pp. 1–16.

[16] Houpt, A. and Leonov, S., "Cylindrical Focused Laser Differential Interferometer," *AIAA Journal*, Vol. 59, No. 4, 2021, pp. 1142–1150.

[17] Shine, J., White, J., Bowersox, R. D., White, E. B., Gragston, M. T., and Siddiqui, F., *3D-Printed Quasi-Random Distributed Roughness for Turbulent Boundary Layer Analysis on Hypersonic Ogive Nosecones*, 2023.

[18] Benitez, E. K., Ceruzzi, A., Gragston, M., Parziale, N. J., Schmidt, B. E., and Weisberger, J. M., "Focused Laser Differential Interferometry: Recent Developments and Applications for Flow Measurements," *AIAA SCITECH 2025 Forum*, American Institute of Aeronautics and Astronautics, Reston, Virginia, 1 2025.

[19] Neet, M. C., Lawson, J. M., and Austin, J. M., "Design, alignment, and calibration of a focused laser differential interferometer," *Applied Optics*, Vol. 60, 9 2021, pp. 7903.

[20] Born, M. and Wolf, E., *Principles of Optics: Electromagnetic Theory of Propagation, Interference and Diffraction of Light*, Cambridge University Press, Cambridge, UK, 7th ed., Oct. 13 1999.

[21] Ceruzzi, A. P. and Cadou, C. P., "Interpreting single-point and two-point focused laser differential interferometry in a turbulent jet," *Experiments in Fluids*, Vol. 63, 7 2022.

[22] Ceruzzi, A. P., Le Page, L. M., Kerth, P., Williams, B. A. O., and McGilvray, M., "Simultaneous measurements of freestream disturbances, boundary layer instabilities and transition location on moderately blunt cones," *AIAA SciTech Forum and Exposition, 2024*, American Institute of Aeronautics and Astronautics, 2024.